THE JOURNAL OF PHYSICAL CHEMISTRY C

Article

Cite This: J. Phys. Chem. C 2017, 121, 28527−28536

pubs.acs.org/JPCC

Methane Flow through Organic-Rich Nanopores: The Key Role of Atomic-Scale Roughness

M. F. Castez,[†,‡,§] E. A. Winograd,[*,†] and V. M. Sánchez[‡,∥,⊥]

[†]YPF Tecnología S.A., Avenida del Petróleo s/n, 1923 Berisso, Buenos Aires, Argentina

[‡]Consejo Nacional de Investigaciones Científicas y Técnicas (CONICET), Godoy Cruz 2290, 1425 Ciudad de Buenos Aires, Argentina

[§]Universidad Nacional de La Plata (UNLP), Avenida 7 877, 1900 La Plata, Buenos Aires, Argentina

[∥]Centro de Simulación Computacional para Aplicaciones Tecnológicas, CSC-CONICET, Godoy Cruz 2390, 1425 Ciudad de Buenos Aires, Argentina

[⊥]ECyT, UNSAM, 25 de Mayo y Francia, 1650 San Martín, Argentina

ABSTRACT: We perform a detailed study of methane flow through nanoporous kerogen. Using molecular dynamics and modeling the kerogen pore with an amorphous carbon nanotube (a-CNT), we show that the reported flow enhancement over Hagen−Poisseuile flow is mainly due to the smoothness, on an atomic scale, of the CNTs. It acts in two ways: first, it helps the mobility of the adsorbed layer; second, and even more important for the flow enhancement, it prevents the dependency on the inverse of the channel length (L) from developing. While the former can incrementally contribute to the flow, the latter effect can explain the orders of magnitude found in comparison to macroscopic results.

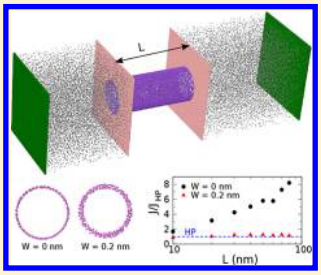

1. INTRODUCTION

Global energy demand is continuously increasing along with the exhaustion of conventional hydrocarbon resources, driving the necessity of developing alternative energy resources. In this context, unconventional hydrocarbon reservoirs become an important source to mitigate this issue. In fact, nowadays, shale reservoirs are commercially viable, which makes them attractive for oil and gas companies, despite the fact that many important challenges concerning their exploitation remain unclear and are the focus of current research.

Shale reservoirs are substantially different from the conventional ones, and one of their distinctive characteristics is the presence of organic matter (kerogen) of extremely low permeability. While kerogen's structure may be complex,[1] it is mainly constituted by heavy insoluble organic compounds which trap the lighter hydrocarbons inside their pores. An important fraction of its porosity lies in pores in the range of the nanometers.[2] When these pores are connected with the well through a highly conductive channel (as, for instance, one created by a hydraulic fracture), they may then contribute to the overall production of the well.

While flow on the porous matrix is well understood for conventional reservoirs by means of the Darcy equation, it is still unclear how to model such a process in shale. The presence of both organic and inorganic (mineral) matter in the rock, which have different affinities for hydrocarbons and water, the sorption of the fluid in the matrix, the nanoscale size of the pores, etc. are some of the sources of uncertainty and difficulty concerning its modeling.

Regarding flux on the nanopores of kerogen, experimental studies on carbon nanotubes (CNTs), which constitute a simplified model for kerogen pores, have shown that the flow rate in such conditions can be orders of magnitude higher than that predicted from macroscopic laws. The reported enhancement varies according to the fluid, CNT radius (R), and experimental conditions, ranging from 1 to 2 orders ($R \approx 20$ nm),[3] 2−3 orders ($R \approx 1$ nm),[4] and 4−5 orders ($R \approx 3.5$ nm).[5] At these scales, the continuum approximation is challenged as the characteristic length of the geometrical system (R in the case of CNTs) is comparable to the mean free path (λ) of the fluid molecules. This is measured in terms of the Knudsen number (K_n)

$$K_n = \frac{\lambda}{R} \tag{1}$$

Different flow regimes can be found from the continuum limit, captured by Navier−Stokes equations ($K_n \to 0$), to the free molecular flow when $K_n \gg 1$.

However, the description of hydrocarbon flow in unconventional reservoirs is still influenced by the classical description of conventional reservoirs, and the Darcy law remains the main equation for this modeling, due to the lack of analytical models covering all relevant scales. In this context, and for the sake of future comparison, we introduce here a brief description of some simple continuum models of fluid flow.

From the point of view of the classical continuous description of Newtonian fluids and under the assumption of a parallel laminar flow (in which case the convective term in the

Received: October 3, 2017
Revised: December 1, 2017
Published: December 1, 2017

DOI: 10.1021/acs.jpcc.7b09811
J. Phys. Chem. C 2017, 121, 28527−28536

Navier−Stokes equation becomes negligible), a fluid of dynamic viscosity μ flowing through a cylindrical channel of radius R and length L subject to a pressure drop ΔP between both ends develops, in the steady-state, a radial velocity profile given by

$$v_x(r) = \frac{\partial P}{\partial x}\frac{r^2}{4\mu} + C \tag{2}$$

where we have assumed than the channel is disposed along the x-axis and r is the radial coordinate. The integration constant C in eq 2 can be obtained if the boundary condition for the velocity at the wall is known, i.e, if $v_x(R)$ is known. For ordinary macroscopic cases (as in pipelines), the so-called "nonslip boundary condition" $v_x(R) = 0$ is an excellent approximation, from which the volumetric flow rate Q can be obtained by performing an elementary integration through the channel cross-section:

$$Q = \frac{\pi}{8\mu}R^4\frac{\Delta P}{L} \tag{3}$$

where a constant pressure gradient along the channel is assumed, $\partial P/\partial x = -(\Delta P/L)$, $\Delta P = P_> - P_<$ being the pressure drop between channel ends (we are calling $P_>$ and $P_<$ the pressure values at the high- and low-pressure reservoirs, respectively). Equation 3 is the well-known Hagen−Poiseuille (HP) relationship.

On the other hand, for channel radii in the (sub)micrometer range, the nonslip boundary condition often becomes unappropriated. Under these conditions, the Knudsen number is around 0.1, which could imply either a slip flow or a transition flow regime.[6,7] In such cases, the velocity near the channel wall is non-negligible, and it is usually better to impose the so-called "slipping boundary condition" in which

$$v_x(R) = -\lambda_s \left.\frac{dv_x}{dr}\right|_{r=R} \tag{4}$$

where λ_s has length units and is referred to as the *slip length*. Applying this boundary condition, we can obtain the volumetric flow rate under slipping conditions:

$$Q_S = \frac{\pi}{8\mu}(R^4 + 4\lambda_s R^3)\frac{\Delta P}{L} \tag{5}$$

We shall refer to eq 5 as the "slipping Hagen−Poiseuille" (SHP) relationship.

While HP and SHP usually correctly describe the flow of Newtonian fluids in channels of dimensions larger than microscale, the flow in channels of dimensions on the submicrometer and nanometer scales is more complex. In particular, confinement and surface effects in nanochannels entail that the viscosity of the nanoconfined fluid does not equal the bulk viscosity.[8] Even more dramatically, the proper continuous assumption in these nanofluidic systems is no longer valid. The number of particles involved in such mass transport processes is far below the typical macroscopic analogues, and fluctuations inherent to every discrete system[9] are usually important. However, due to the lack of relationships adequate for nanofluids, it is a regular practice to extrapolate the scope of HP and SHP to be applied to nanofluidic systems.[8,10,11] Following such a procedure, in this work, we invoke the HP and SHP models several times, for the sake of comparison, relating numerical molecular dynamics results to well-known theoretical models.

The inapplicability of continuous fluid mechanics in nanoscale systems makes numerical methods such as molecular dynamics (MD) an attractive alternative. In this regard, we perform an exhaustive MD study on the transport of methane through carbon nanochannels driven by pressure gradients.

In the past few years, many related papers have been published, usually modeling kerogen's nanopores by a smooth graphene slit or tube, with high- and low-pressure reservoirs at the two ends. In refs 12 and 13, using the dual-control volume grand canonical molecular dynamics (DCV-GCMD) implementation to generate a pressure difference between reservoirs, Jin and Firoozabadi state that flow enhancement of methane is due to an adsorbed layer of mobile molecules, which generate heterogeneities on the density distribution, which have no equivalence in HP-like flows. In ref 14, Riewchotisakul and Akkutlu used a mobile piston to drive the flow between the reservoirs to conclude, in a similar way, the existence of flow enhancement due to the adsorbed layer, although they obtained an enhancement of as much as 1 order of magnitude higher than the HP prediction. Wang et al.[15] and Feng and Akkutlu[10] also reported the presence of adsorbed mobile layers which contribute to the flow. In these studies, external force fields were applied on fluid molecules to account for the pressure gradient.

In ref 10, the authors considered surface roughness, including periodically distributed carbon-based rings inside the nanopore. They show that while the density profile is mildly affected, the velocity of the adsorbed layer strongly decreases, but remains finite. In ref 16, Joseph and Aluru studied the effect of roughness on water transport in CNTs and showed that flow enhancement is suppressed, due to the disturbance of the molecular bonds. Ho et al., in ref 17, showed that the relation between the interatomic distance of surface atoms, a natural length scale of surface roughness, and the size of the fluid molecules plays an important role concerning the flow slippage.

As has been pointed out in the literature,[1,18] kerogen is constructed by organic macromolecules which are randomly orientated and make up a complex structure. The porosity naturally emerges from the randomness of this arrangement. Therefore, in contrast with the cited papers, in this work we consider amorphous carbon nanotubes (a-CNTs) to describe in a more realistic way pore throats found in shale. We also include roughness on the nanopore, in a way different from that of ref 10, that we think is a closer description of real systems.

Doing computationally demanding MD simulations, we show how analytical results from the continuum limit (Knudsen diffusion, HP, or SHP, for example) emerge from molecular dynamics, which helps us to identify that the main driver of flow enhancement is the surface smoothness at the atomic scale. In fact, we show how the atomic-scale surface roughness strongly affects the mobility of the adsorbed layer (as stated in ref 10) but, more dramatically, completely modifies the dependence of the flow on the pore length (L).

It is important to mention that several authors have pointed out the importance of low friction on the flow enhancement, in particular, regarding water flow in CNTs. In ref 19, Chen et al. argue that the effective viscosity decreases as a consequence of the confinement and flow rate. In ref 20, Kannam et al. compute the slip length in the nanotube, which can be about 2 orders of magnitude higher than the nanotube diameter. In ref 21, Falk et al. discuss the influence of the tube curvature on the water−wall friction and find that, for CNTs, it can vanish for small enough radii. None of these studies had explicitly

DOI: 10.1021/acs.jpcc.7b09811
J. Phys. Chem. C 2017, 121, 28527−28536

considered fluctuations in the lattice positions of the atoms of the CNT, as done in this work, which is a natural source of surface roughness, which allow us to identify the particular dependence of the flow on the pore throat length.

The rest of the paper is organized as follows: In section 2, we present a detailed description of the implemented model and relevant methods. In section 3, we introduce the main results of this study. In section 3.1, we discuss the effects of considering an a-CNT as opposed to an ideal one, in section 3.2, we include the surface roughness and benchmark our results with analytical models, for low and high pressures, and in section 3.3, we discuss the strong effects of surface roughness on the dependence of the flow rate on the pore throat length. Finally, in section 4 we present the concluding remarks.

2. METHODS

We use LAMMPS[22] for performing nonequilibrium molecular dynamics (NEMD) simulations of methane transport through carbon nanochannels. Molecular dynamics is a numerical technique to solve the evolution equations (the Newton equations in the case of classical systems) of an ensemble of interacting particles. For the sake of computational speed, and to let us consider larger systems (therefore improving our results in a statistical sense), we have chosen do not consider internal degrees of freedom of methane molecules, but consider methane as a point particle. The interaction between a pair of molecules is described by the Lennard-Jones interaction potential[23]

$$V_{LJ}(r) = 4\epsilon\left[\left(\frac{\sigma}{r}\right)^{12} - \left(\frac{\sigma}{r}\right)^{6}\right] \quad (6)$$

where ϵ is the depth of the potential well and σ is related to the distance at which $V_{LJ}(r)$ takes its global minimum r_{eq} through $r_{eq} = 2^{1/6}\sigma$.

Our simulation box consists of three parts: a high-pressure reservoir, a low-pressure reservoir, and a nanochannel region. Pressure in each reservoir is controlled by means of two independent pistons submitted to external forces (computed as the desired target pressure times the piston area), while temperature is controlled applying a Nosé−Hoover[24,25] thermostat. We choose a coordinate system in which the x-axis is parallel to the nanochannel axis. Periodic boundary conditions are only imposed along the y- and z-axes. Along the x-axis, the piston positions are constrained to the box length, and the simulation ends if a piston reaches a box boundary.

The simulation is divided into two stages. During the first one, the *equilibration stage*, the nanochannel is closed and no particle can migrate from one reservoir to the other. During the second one, the *transport stage*, the nanochannel is opened and the mass transfer process begins. A complete picture of the modeled system is shown in Figure 1a. For visualization purposes, we show a small system in which each reservoir has a volume of $10 \times 7 \times 7$ nm^3. However, typical volumes we used were about $150 \times 15 \times 15$ nm^3 to increase the number of particles.

Initially, methane molecules are inserted into each reservoir at a density consistent with the external pressure imposed in each reservoir and the target temperature (throughout this paper, all MD simulations have been performed at the temperature $T = 400$ K; i.e., we are working with a supercritical fluid). The initial particle density for each reservoir was estimated by means of the Peng−Robinson equation for methane.[26]

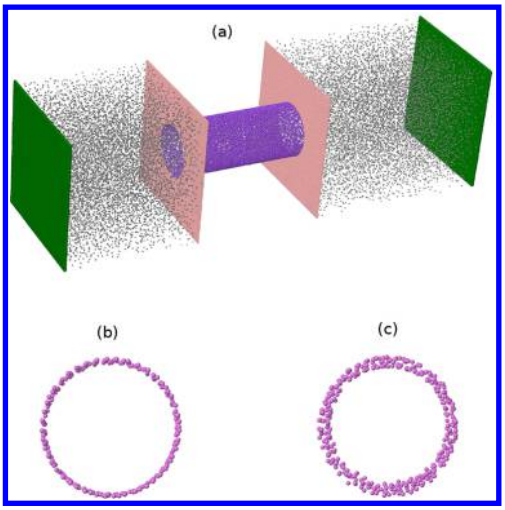

Figure 1. (a) View of the simulated system: Two reservoirs containing methane particles (gray) are joined by a cylindrical nanotube (violet), while independent pistons (green) perform pressure control in each reservoir. Pink particles constitute the reservoir walls. (b) Cross-sectional view of an atomically smooth nanotube ($W = 0$). (c) Cross-sectional view of an atomically rough nanotube ($W = 0.1$ nm).

Walls in our system (pistons, reservoir walls, and nanochannel) are made of point particles. Particles from the reservoir walls and from the nanochannel are immobile,[27] while each piston moves as a rigid body. The interactions between methane molecules and piston particles and between methane molecules and reservoir walls have, in our model, the only purpose of confining methane molecules, so we have employed unspecific short-range Lennard-Jones potentials to describe such interactions ($\sigma = 0.15$ nm and $\epsilon = 0.01$ kcal/mol). Moreover, the mass of the particles that constitute the pistons are light enough (0.1 Da) to allow the pistons to quickly compensate for reservoir pressure fluctuations. The only relevant specific interactions in our model are the methane−methane and methane−carbon interactions. We employ Lennard-Jones parameters according to the OPLS-UA potential database[28,29] in which $\epsilon_{CH_4-CH_4} = 0.2941$ kcal/mol, $\epsilon_{CH_4-C} = 0.1225$ kcal/mol, $\sigma_{CH_4-CH_4} = 0.3730$ nm, and $\sigma_{CH_4-C} = 0.3617$ nm.[30] All LJ cutoffs were set to 2.5σ.

Amorphous nanotubes in our system are generated by disposing carbon atoms randomly on a cylinder of imposed radius R and length L until their amount matches the cylinder area ($2\pi RL$) times the graphene particle areal density, 38 nm^{-2}. During the atom insertion process, the distance between first neighbor carbon atoms is constrained to be higher than a threshold value of 0.13 nm. Proceeding in this way, we generate what we call "smooth" nanotubes: all carbon atoms lie on a geometrically perfect cylinder. On the other hand, what we shall call "rough" nanotubes are generated by simply adding a random radial shift δ_r over each particle in the nanotube, with $\delta_r = x_r W$, where x_r is a random variable uniformly distributed in $[-0.5, +0.5]$ and W is a parameter that allows us to control the amplitude of fluctuations ($W = 0$ corresponds to a smooth nanotube), i.e., allowing us to control the surface roughness (see Figure 1b). It is evident that W cannot be arbitrarily large, taking into account that we do not desire methane filtering through the surface of the nanotube. Therefore, in this work, W

DOI: 10.1021/acs.jpcc.7b09811
J. Phys. Chem. C 2017, 121, 28527−28536

varies in the range of 0−0.2 nm. Figure 1c shows a cross-sectional view of a rough nanotube with W = 0.1 nm.

During the equilibration stage, piston oscillations are weakened, including damping forces. Once the volumes reach steady-state values, the system is considered equilibrated, the nanochannel is opened, and the transport stage begins. During the transport stage, damping forces on the pistons are switched off. A picture of the overall scheme is shown in Figure 2.

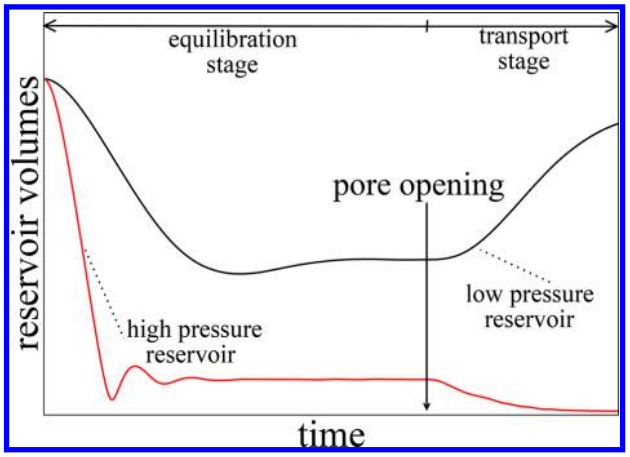

Figure 2. Schematic view of the different stages in the simulation: initially (*equilibration stage*), the pore remains closed (no particle exchange takes place between the reservoirs). Once the gas pressure equilibrates against the pressure externally imposed through the pistons, the pore is opened and the particle exchange between the reservoirs starts (*transport stage*).

In most of the MD simulations presented in this paper, the total number of methane particles incorporated ranges between 1 million and 3 million, and the overall simulated time ranges between 3 and 10 ns.

The nanotube remains empty during the equilibration stage. When the transport stage begins, mass density inside the nanotube increases until it reaches a steady state, performing fluctuations around a saturation value. On the other hand, mass density inside the nanotube is inhomogeneous, being higher near the nanotube wall, indicating the formation of an adsorbed layer.[10,12,15] We follow up the evolution of mass density in several control annular regions of the nanotube during the whole transport stage, which allows us to obtain velocity and density profiles. As the number of particles in some of these control regions at a given time can be small, time averaging over relatively long times (typically, a few nanoseconds) is necessary to acquire reasonable statistics. In agreement with previous results,[31] we observed that the mass density in each region is maintained during the flow process, fluctuating around steady-state values (Figure 3). In the regimes studied here, it is possible to identify two regions: an adsorbed region near the pore walls and a center region,[10] with a density similar to that corresponding to the bulk. The adsorbed layers are created as a consequence of the pore wall−hydrocarbon attraction. The precise density values in the adsorbed region depend on the temperature and pressure.[31,32]

During the transport stage, we compute the molecular flow by measuring the difference in the number of molecules in the low-pressure reservoir ($N_<$) and its initial number ($N_<(t{=}0)$). In Figure 4, we show the typical time evolution of $\Delta N(t) = N_<(t) - N_<(0)$ for different values of the nanotube radius R.

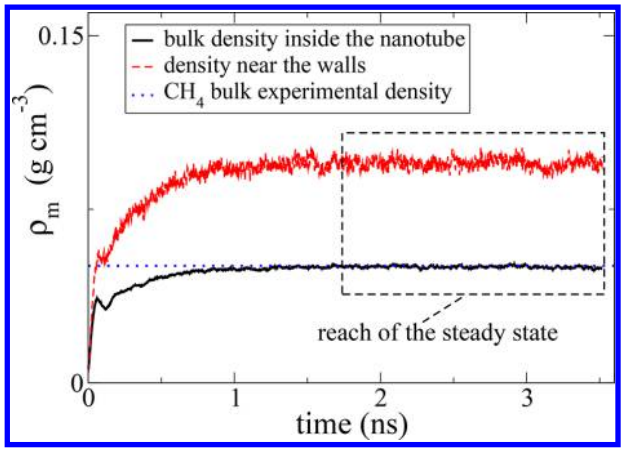

Figure 3. Mass density inside the nanotube increases to reach a steady state, performing fluctuations around a saturation value. The mass density is higher near the nanotube wall, indicating the formation of an adsorbed layer.

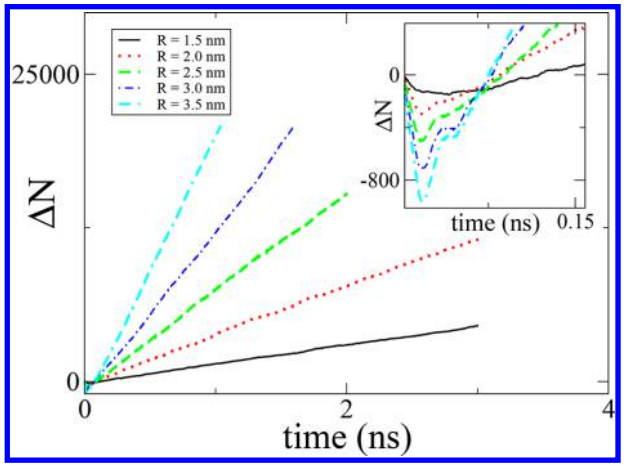

Figure 4. After the time needed to reach the steady state, ΔN increases linearly with time. Notice that negative values of ΔN are obtained in a short initial transient stage (inset) that corresponds to the filling of the initially empty nanotube.

We can see in the inset of Figure 4 that there is a short transient in which $\Delta N(t)$ becomes negative, corresponding to the filling of the nanotube. Once this transient has elapsed, $\Delta N(t)$ increases linearly with time.[33] Within this linear region, we define the overall flow J (number of particles entering the low-pressure reservoir per nanosecond) as the slope of the ΔN vs t plot. We keep track of the densities (see Figure 3) and velocities inside the nanotube and also of the pressures in the reservoirs to correctly determine the linear regime of the steady state.

3. RESULTS AND DISCUSSION

3.1. Amorphous versus Graphitic CNTs. Most of the related studies reported in the literature model the kerogen's pore throats with a graphitic CNT.[10,19,21] However, such perfect structure is hard to expect in shales at reservoir conditions, since kerogen is composed by randomly oriented organic macromolecules with pores inside.[1,18] An amorphized form of graphene, which is the one used throughout this work, should be more realistic.

To analyze the differences of considering any of the two nanotubes, we built up graphitic and amorphized tubes with the

DOI: 10.1021/acs.jpcc.7b09811
J. Phys. Chem. C 2017, 121, 28527−28536

same length and radius; graphitic nanotubes were of the armchair type, while the amorphized nanotubes were of the smooth type ($W = 0$). Snapshots of the nanotubes are shown in Figure 5.

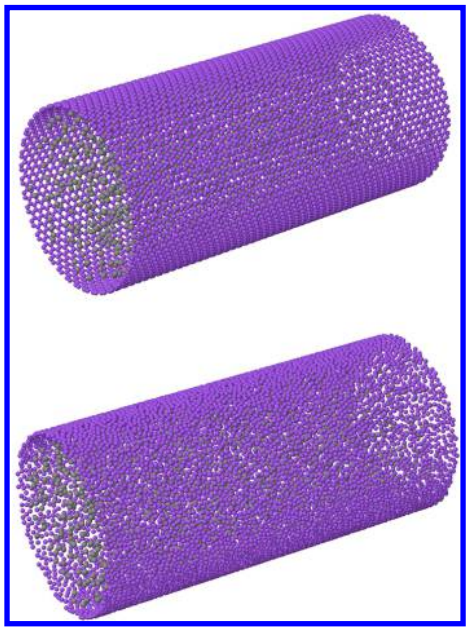

Figure 5. Snapshots of crystalline (top) and amorphous (bottom) nanotubes.

In Figure 6, we plot the molecular flow on both types of nanotubes for different geometrical dimensions R and L and

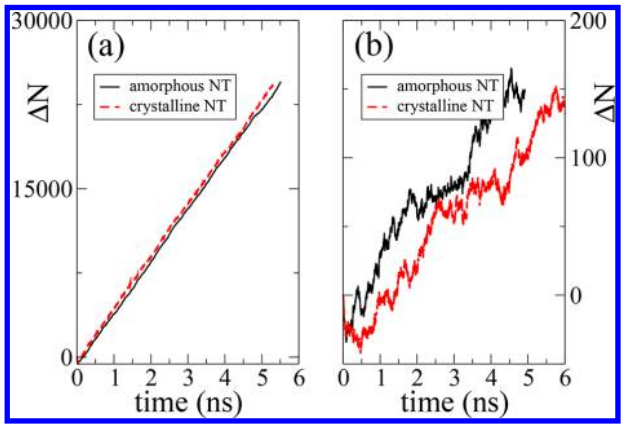

Figure 6. Time evolution of ΔN for a perfect graphitic nanotube, CNT (dashed lines), compared to the flow obtained with an amorphous smooth nanotube, a-CNT ($W = 0$) with the same geometrical parameters L and R (solid lines). Results in (a) correspond to parameters $L = 12.375$ nm, $R = 2.712$ nm, $P_> = 475$ atm, and $P_< = 425$ atm. Data shown in (b) correspond to parameters $L = 24.472$ nm, $R = 0.814$ nm, $P_> = 110$ atm, and $P_< = 90$ atm.

under different conditions of mean pressures $P_m = (P_> + P_<)/2$ (pressure values on the order of typical reservoir conditions), where we can see that the main characteristics of the flow are insensitive to the long-range order of the graphitic nanotube. This result shows that breaking this order, although constraining the atomic positions to the nanotube cylinder, does not cause any important change in the flow properties. Contrarily, in the following sections, we will show that fluctuations along the radial coordinate (controlled by the surface roughness parameter W) are essential to understand the many-orders enhancement in flow rates found in the experiments.

3.2. Connection to the Macroscopic Limit. To check the robustness of the numerical implementation, we have considered several limits, which allow us to compare our simulations with known analytical results.

While analytical models predict a linear dependency of the flow rate on the pressure drop, it is not evident that, in a general case, the MD simulations will capture this behavior and that, for low enough R, surface effects will not change this relationship.

In Figure 7, we plot the molecular flow rate (J) variation with ΔP for two extreme values of the mean pressure P_m and over a

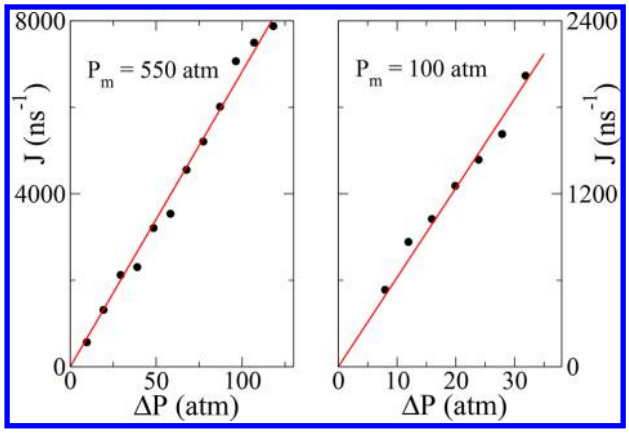

Figure 7. Numerical results showing the proportionality between the measured flow J and the pressure drop ΔP for $P_m = 550$ atm (on the left) and $P_m = 100$ atm (on the right). The former corresponds to a nanotube of $R = 2.5$ nm and $L = 25$ nm and the latter to a nanotube of $R = 3$ nm and $L = 30$ nm.

wide range of pressure drops. In agreement with HP and SHP, we find that the linear dependence still holds in the simulated conditions.

In the following sections, we benchmark our results at low and high pressures with analytical models.

3.2.1. Low-pressure limit. As a further step in the validation of the model, we have considered the low-pressure limit, in which it is possible to compare our results with the Knudsen diffusion equation.

At low pressures, methane at 400 K can be thought of as an ideal gas with a Knudsen number $K_n \gg 1$. This means that the probability of molecule−molecule collisions inside the channel is small. Molecules inside the nanotube effectively interact only with the nanotube wall. In fact, following the trajectory of a single molecule (Figure 8), we can observe that it performs long rectilinear paths until being reflected in some direction. It can also be observed that it eventually experiences an adsorbed transient stage during collisions, but most of the time it is traveling.

This picture allow us to identify two limiting cases: If the reflections are exactly specular, we can estimate the particle flow by considering the classical analogue problem of the effusion of ideal gases.[34] On the opposite limit, if all reflections are diffusive, the net particle flow can be estimated through the Knudsen equation.[35,36] However, reflections of methane molecules with the carbon nanotube walls are neither perfectly

DOI: 10.1021/acs.jpcc.7b09811
J. Phys. Chem. C 2017, 121, 28527−28536

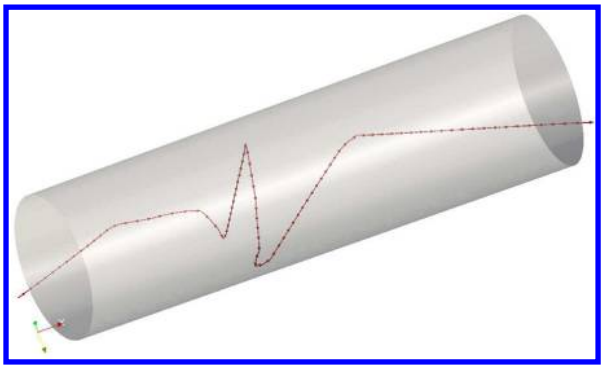

Figure 8. Trajectory of a single particle traveling across a rough nanotube (W = 0.2 nm) in the $K_n \gg 1$ regime, in which methane–methane collisions are much less frequent than methane–nanotube wall collisions.

specular nor perfectly diffusive. We expect that the fraction of diffusive reflections grows as the nanotube roughness W increases. Taking into account these considerations, we conjecture that, with increasing nanotube roughness W, we can approach the Knudsen regime, while, for W = 0 and small channel lengths L (to decrease the probability of diffusive reflections), we approach the effusion case. This predicted behavior effectively holds, as can be seen in Figure 9. In

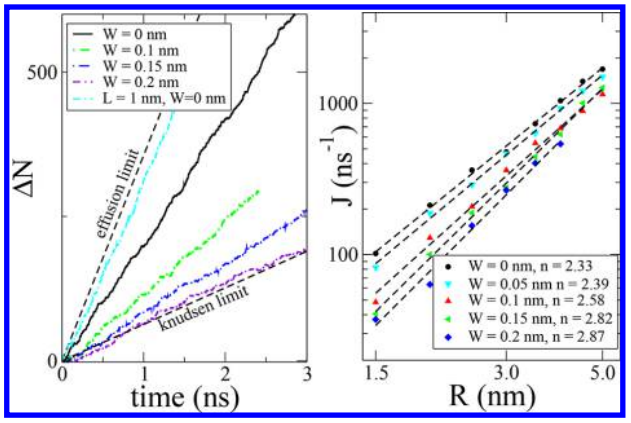

Figure 9. Left: Time evolution of ΔN for nanotubes with different values of the atomic scale roughness W ($P_>$ = 9 atm and $P_<$ = 1 atm). As W increases, diffusive reflections dominate and the Knudsen flow regime is approached. For low values of roughness and short nanotubes, the contribution of diffusive reflections is negligible and flow approaches the effusion limit. Right: Log–log plot of the flow J as a function of the nanotube radius for different values of W. Values of the n exponent fitted according to the power law $J \propto R^n$ are indicated in the legends. Unless otherwise indicated, in these simulations, L was set to 30 nm.

particular, on the right side of Figure 9, we can see that the particle flow J in the simulations follows a power-law behavior as a function of the nanotube radius ($J \propto R^n$) and that the exponent n grows from values near 2 (expected exponent in a pure effusion process) toward values near 3 (expected exponent according to the Knudsen equation) as the nanotube roughness W increases.

3.2.2. High-Pressure Limit. Flow rates from classical models such as HP (eq 3) and SHP (eq 5) are obtained under the underlying assumption of a constant radial particle density. However, this picture, very intuitive at the macroscale, does not hold at the nanoscale. We now examine the behavior of the density profile as R increases. It is trivial to notice that when the channel diameter is lower than the molecular diameter, no flow can take place, despite the fact that HP and SHP predict nonvanishing flow for any nonzero R. When R becomes slightly larger than the characteristic length for the methane–wall interaction,[37] flow arises and the radial particle density $\rho_p(r)$ exhibits a peak centered in the middle of the channel (see Figure 10a).[38] As R increases, the particle density at the center

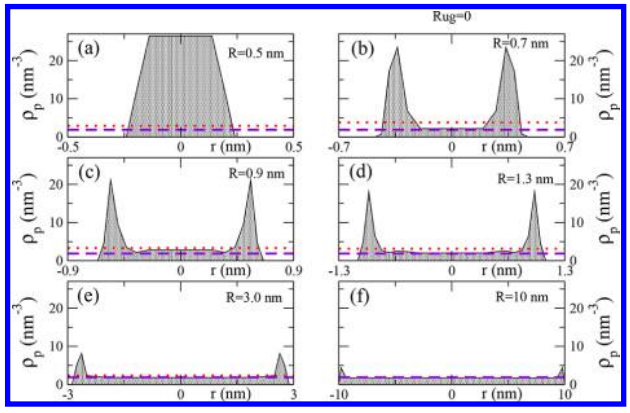

Figure 10. Particle radial densities inside the nanotube for different radii. Dotted lines correspond to the average particle densities inside the nanotube, while dashed lines indicate the bulk densities. Data correspond to a smooth nanotube (W = 0) with L = 30 nm, and pressures in the reservoirs were $P_>$ = 110 atm and $P_<$ = 90 atm.

decreases, while it is enhanced next to the channel's wall. This high-density layer is usually called the *adsorbed layer* (AL). It is important to stress that, for a small channel radius ($R \lesssim 3$ nm, for instance), a large fraction of the particles inside the channel are in the AL, which is a completely different scenario from that considered by the HP and SHP models. As R further increases, the adsorbed layer is still observable, surrounded by a few layers showing small oscillations around a certain value that is increasingly similar (according R grows) to the bulk particle density. For high enough R, the fraction of particles in the AL becomes negligible with respect to the total number of particles in the channel. The described behavior is summarized in Figure 10), which agrees with previously reported results.[15]

Therefore, at relatively high R (for instance, $R \approx 10$ nm), continuous models such as HP and SHP can be reasonably applied to describe the flow, in the sense that (1) the number of particles inside the channel in a typical case is more compatible with the continuous assumption and (2) the adsorbed layers do not involve a number of particles that seriously alters the assumption of a homogeneous radial density.

To account for heterogeneities inside the pore matrix, we studied the effect of roughness present at the nanoporous carbon wall. The first remarkable consequence of adding roughness to the system is the decrease of methane flux.[10] Interestingly, we find that, for both smooth and rough nanotubes, the main flow characteristics (for $R \gtrsim 10$ nm) can be reasonably described by means of the SHP model. However, the value of the slip length is very sensitive to the value of the roughness W, decreasing as W grows. These can be seen in Figures 11 and 12. For a smooth nanotube (W = 0), a parabolic velocity profile for the component along the nanochannel axis V_x was obtained in the steady state, but a slip length λ_s = 6.8 nm was needed to satisfy the nonvanishing velocity on the nanotube wall, as can be seen in the inset of Figure 11. By

DOI: 10.1021/acs.jpcc.7b09811
J. Phys. Chem. C 2017, 121, 28527–28536

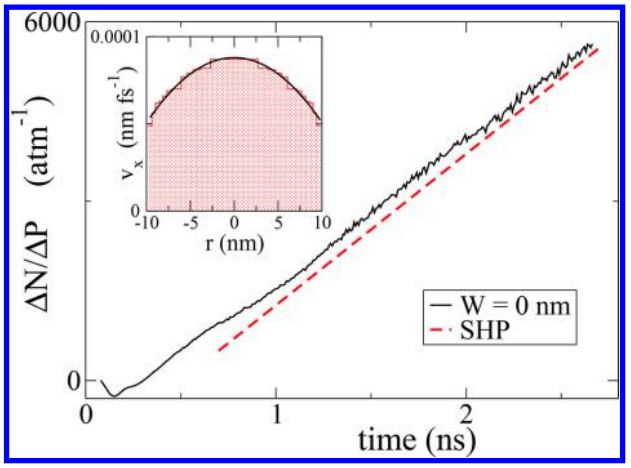

Figure 11. Time evolution of ΔN per unit pressure drop for a smooth nanotube (W = 0) with L = 30 nm, R = 10 nm at P_m = 100 atm and ΔP = 20 atm. The solid line corresponds to the simulated data, and the dashed line corresponds to the expected evolution for $\Delta N/\Delta P$ according to the SHP eq 5 with the slip length λ_s = 6.8 nm, a value obtained by fitting the simulated velocity profile to the SHP theoretical profile, as shown in the inset.

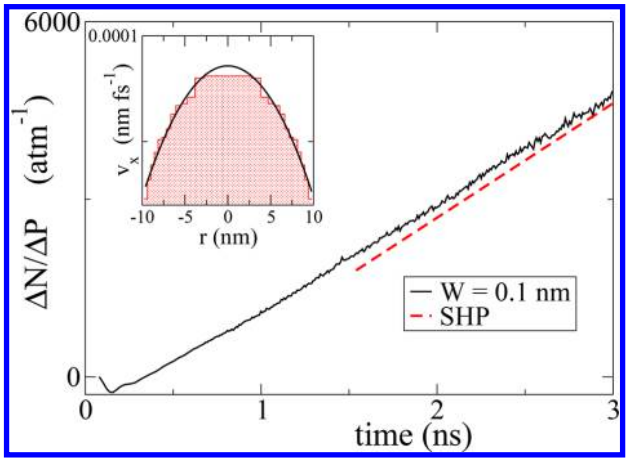

Figure 12. Time evolution of ΔN per unit pressure drop for a rough nanotube (W = 1) of length 30 nm and radius 10 nm at P_m = 100 atm and ΔP = 20 atm. The solid line corresponds to the simulated data, and the dashed line corresponds to the expected evolution for $\Delta N/\Delta P$ according to the SHP eq 5 with the slip length λ_s = 1.9 nm, a value obtained by fitting the simulated velocity profile to the SHP theoretical profile, as shown in the inset.

using the fitted λ_s and experimental values of the bulk viscosity and density for methane,[39] we verified that the growth rate of ΔN is well described by the SHP model (solid and dashed lines in Figure 11).

The same procedure was applied to a rough nanotube (W = 0.1 nm), with the only difference that the slip length was severely reduced to λ_s = 1.9 nm, as can be seen in Figure 12. It is important to notice that the strong changes in the flow characteristics (such as the slip length) induced by increasing the nanochannel roughness are not reflected in the density profiles, since they are almost indistinguishable for both cases (W = 0 and W = 0.1 nm), as can be seen in Figure 13.

Reported values of the slip length can be found in refs 15 (for hydrocarbons) and 20 (for water). While the precise value depends on the particular thermodynamic conditions and on the characteristics of the CNT and fluid involved, our obtained

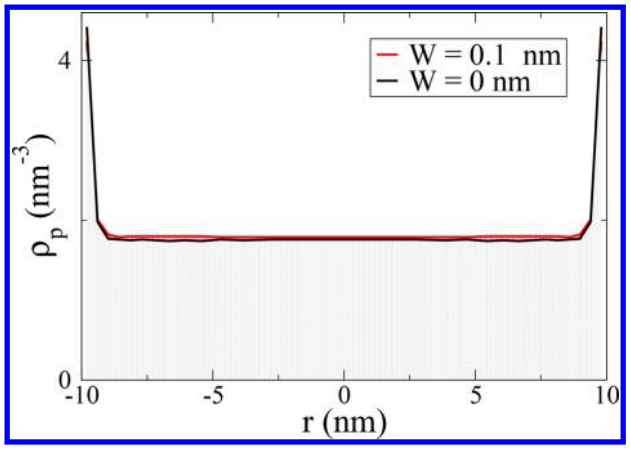

Figure 13. Particle radial densities inside the nanotube for the cases shown in Figures 11 and 12, showing that, when the nanotube radius is relatively large, the nanotube roughness does not have a strong impact on the radial distribution of particles.

λ_s values follow the same trend as those described in published numerical papers.

For the case of smaller R, we find that the particle flow J scales as R^n, with $3 < n < 4$, consistent with the SHP eq 5 in which, for $\lambda_s/L \gg 1$ ($\lambda_s/L \ll 1$), the R^3 (R^4) behavior dominates. In fact, the numerical values for the n exponent increase when W grows, in a way compatible with the fact, already discussed, that the slip length λ_s decreases when W grows. These findings can be seen in Figure 14.

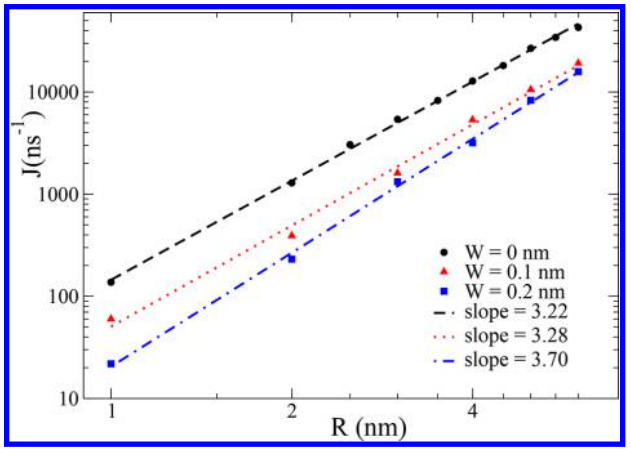

Figure 14. Dependence of the methane particle flux on the radius for three values of the roughness parameter W. Numerical data were fitted with power-law dependencies (viewed as straight lines in the log−log plot), whose exponents are indicated through the slope values. The remaining parameters are L = 10 nm, $P_>$ = 575 atm, and $P_<$ = 525 atm.

3.3. Atomic-Scale Roughness Effects. In the previous section, we showed that roughness, even on an atomic scale where W/R is in about the range of 1−10%, has an important impact on the flow rate, specially acting on the dynamics of the adsorbed layers and altering the slip length. For instance, in Figure 15, we plot the flow rate normalized with the one expected from HP flow for different values of W. It can be seen that, for a smooth nanopore (W = 0), the flow J can be about 5 times higher than J_{HP} (for a specific geometry of the nanochannel, as indicated in the figure). As W increases, the enhancement is reduced and the flow in the nanopore becomes

DOI: 10.1021/acs.jpcc.7b09811
J. Phys. Chem. C 2017, 121, 28527−28536

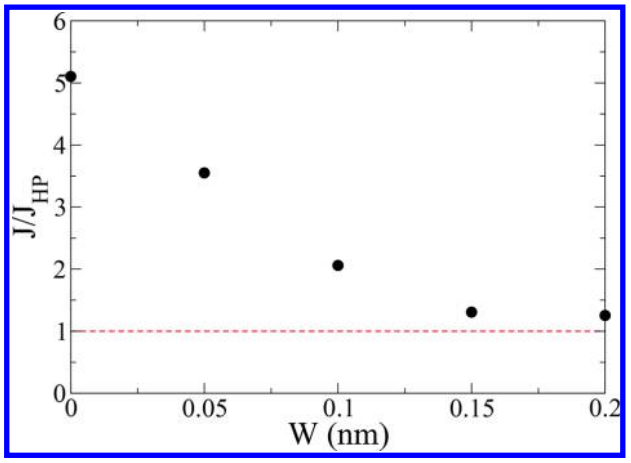

Figure 15. Methane flow rate enhancement over HP for different nanotube roughnesses. The enhancement is strongly affected by the value of the nanochannel roughness parameter W. Geometrical parameters of the nanochannel were L = 40 nm and R = 2.5 nm, while reservoir pressures were $P_>$ = 475 atm and $P_<$ = 425 atm.

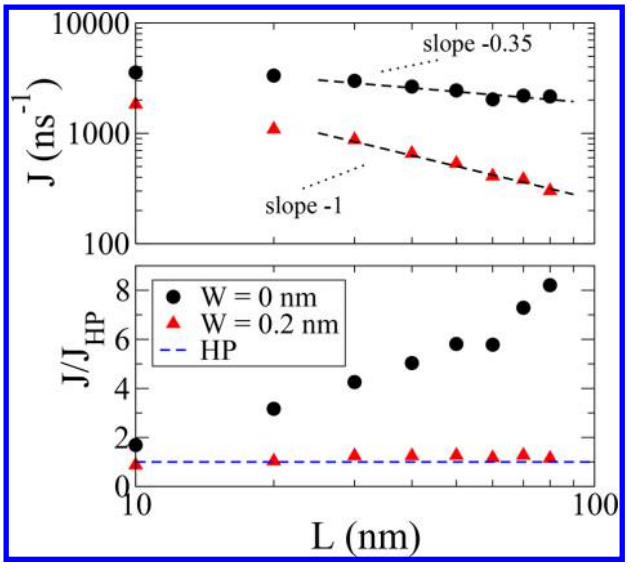

Figure 16. Top: Methane flow rate as a function of the nanotube length L. Notice that, for the rough nanopore (W = 0.2 nm), the inverse dependence on L is achieved for $L \approx$ 30 nm, while the dependence, in the same range, for the smooth nanopore (W = 0), is much lower. Bottom: Flow enhancement compared to HP. While, when W = 0.2 nm, it saturates for $L \approx$ 30 nm, for W = 0, it still increases, showing that finite-size effects are more pronounced at smooth pores and are essential to explain the observed flow enhancement. These simulations correspond to a nanopore of R = 2.5 nm and pressures P_m = 450 atm and ΔP = 50 atm.

closer to that predicted from HP. It is important to emphasize that, even though the overall flow for channels with high enough roughness is quite similar to that predicted by HP, it is incorrect to state that the flow behaves according to that model, since there are other characteristics (such as the inhomogeneous density profile and the strength of the fluctuations, for instance) in which they differ.

In terms of the flow enhancement over HP, a more important effect of surface roughness is how it affects the dependence on the tube length L. From both the HP and SHP macroscopic models, we would expect that, for $R/L \ll 1$, $J \propto L^{-1}$. In our MD simulations, as we implement a finite nanotube where edge effects may become important, it is not evident whether we are capable of reproducing this behavior.

In the top plot of Figure 16, we show the flow rate as a function of L. Interestingly, for the rough nanotube of W = 0.2 nm, the behavior $J \propto L^{-1}$ is achieved for $L \gtrsim$ 30 nm. However, for the smooth nanotube (W = 0), we are not able to obtain that dependence for L in a range amenable for MD simulations ($L \lesssim$ 100 nm). As is shown in that plot, the effect of L on the flow rate for the smooth nanotube is milder than that for the rough one in the same interval. Indeed, the behavior is well fitted by a power law, $J \propto L^{-0.35}$.

This fact has dramatic effects on the enhancement over HP, which is shown in the lower plot of Figure 16. While for the rough nanotube the enhancement is mainly due to the effects of the AL (independent of L for $L \gtrsim$ 30 nm), for the smooth nanotube it continuously grows as L increases, in the manner given by $J(W{=}0)/J_{HP} \propto L^{1-0.35} = L^{0.65}$ (L expressed in nanometers). It is worth mentioning that flow enhancement is even higher for smaller R.

At this point, we are not capable of answering whether this milder dependence on L is a characteristic of the flow rate of smooth CNTs or a finite-size effect that extends much more in L than for a rough nanotube and will eventually become proportional to L^{-1} for long enough tubes. However, whatever the case is, the smoothness of the nanotube plays an essential role in controlling the dependence of the flow on L.

It is interesting that the strong dependence of the flux on L for the perfectly smooth nanotube explains the main differences in the flow enhancement reported in the literature. While the details depend on the exact parameters used to perform the calculations, in ref 13, the authors obtained up to 2 orders of magnitude of enhancement as they increased L (the longest considered nanotube is L = 136.2 nm). In ref 14, the authors obtained a lower enhancement (up to 1 order of magnitude for R = 1 nm). In the latter case, the nanopore length L was set to 10 nm. Considering what we discussed on the flow behavior with L, we can make a rough estimate of the contribution to the enhancement of the dependency on L for the smooth nanopore by considering the scaling $J/J_{HP} \propto L^{0.65}$, obtained for the nanopore of R = 2.5 nm of Figure 16. For L = 136.2 nm, $J/J_{HP} \approx$ 25, while, for L = 10 nm, $J/J_{HP} \approx$ 5. These values are in the same range of the reported values, considering that the mentioned simulations, and those of our work, were performed at different pressures and temperatures.

Moreover, if we use the same argument to account for the enhancement experimentally observed in refs 4 and 40, where they grew CNTs of lengths (radii) $L \approx 5$ μm ($R \approx$ 1.5 nm) and $L \approx 126$ μm ($R \approx$ 3.5 nm), respectively, the expected flow enhancement would be $J/J_{HP} \approx$ 250 in the former case and $J/J_{HP} \approx$ 2000 in the latter case. The reported enhancements are 2−3 and 2−4 orders of magnitude, respectively, in the same orders of the estimations, which also suggests that the contribution to the enhancement may mainly come from the mild dependence on L of finite-sized smooth CNTs. It is important to remark that those experiments were done with fluids, nanotube radii, pressures, and temperatures different from those considered in the present work, so the results should not be quantitatively compared. We do not include the experiment of Whitby et al.[3] as they used wider nanotubes ($R \approx$ 20 nm).

DOI: 10.1021/acs.jpcc.7b09811
J. Phys. Chem. C 2017, 121, 28527−28536

4. CONCLUSIONS

We have performed extensive simulations concerning the flow of methane through amorphous CNTs by means of the MD technique. In a typical case, we simulate systems with several millions of particles, evolving for nearly 10 ns, obtaining good samples (in a statistical sense) for steady-state flow. This study showed overwhelming numerical evidence on how small fluctuations on the radial position of the carbon atoms of the tube, i.e., atomic-scale roughness, dramatically modify the main flow characteristics on nanosized pore throats. While it has a detrimental effect on the flow of the adsorbed layer, its main effect is to quickly recover the dependence of the flow rate on the inverse of the nanotube length L. Therefore, this result indicates that the reported flow enhancement on CNTs[4,5] might be caused by its weak dependence on L, as these CNTs can be considered atomically smooth. We further conjecture that flow enhancement over HP may increase (up to some limit) as L increases. Unfortunately, we are not aware of any experimental study on CNTs with varying L (or, equivalently, the thickness of the CNTs' membranes), which should validate this hypothesis.

By using a rough approximation for the dependence on L of the smooth CNT, we were able to account for the orders of magnitude of flow enhancement reported across many related works.

In light of our results, we consider that the incremental contribution of the adsorbed layer to the flow, which has been suggested as a key point regarding the flow enhancement in CNTs in many related papers,[10,12−14] is not the main reason for such enhancement. The adsorbed layer certainly plays a role in this enhancement, but it is a second-order effect, since its typical density and velocity values are not much higher than those of the bulk. Therefore, its existence cannot explain the several orders of magnitude of enhancement reported in the literature.

Regarding the application of fluid flow in shales, we do not expect to obtain orders of magnitude of enhancement over the predicted behavior, as atomic-scale roughness could be naturally present in kerogen's pores, and the extreme smoothness of CNTs should not be predominant when considering kerogen pore throats.[1,18]

AUTHOR INFORMATION

Corresponding Author

*E-mail: emilio.winograd@ypftecnologia.com.

ORCID

M. F. Castez: 0000-0002-6324-9044

Notes

The authors declare no competing financial interest.

ACKNOWLEDGMENTS

We thank YPF Tecnología S.A. and CONICET (Argentina National Research Council) for their support. This work has been funded by YPF Tecnología S.A.

REFERENCES

(1) Vandenbroucke, M. Kerogen: from Types to Models of Chemical Structure. *Oil Gas Sci. Technol.* **2003**, *58*, 243−269.

(2) Sakhaee-Pour, A.; Bryant, S. Gas Permeability of Shale. *SPE Reserv. Eval. Eng.* **2012**, *15*, 401−409.

(3) Whitby, M.; Cagnon, L.; Thanou, M.; Quirke, N. Enhanced Fluid Flow Through Nanoscale Carbon Pipes. *Nano Lett.* **2008**, *8*, 2632−2637.

(4) Holt, J. K.; Park, H. G.; Wang, Y.; Stadermann, M.; Artyukhin, A. B.; Grigoropoulos, C. P.; Noy, A.; Bakajin, O. Fast Mass Transport through Sub-2-Nanometer Carbon Nanotubes. *Science* **2006**, *312*, 1034−1037.

(5) Majumder, M.; Chopra, N.; Andrews, R.; Hinds, B. J. Nanoscale Hydrodynamics: Enhanced Flow in Carbon Nanotubes. *Nature* **2005**, *438*, 44−44.

(6) Mosher, K.; He, J.; Liu, Y.; Rupp, E.; Wilcox, J. Water Transport through Ultrathin Graphene. *Int. J. Coal Geol.* **2013**, *109-110*, 36−44.

(7) Singh, H.; Javadpour, F. Langmuir Slip-Langmuir Sorption Permeability Model of Shale. *Fuel* **2016**, *164*, 28−37.

(8) Thomas, J. A.; McGaughey, A. J. H. Reassessing Fast Water Transport through Carbon Nanotubes. *Nano Lett.* **2008**, *8*, 2788−2793.

(9) Kampen, N. G. V. *Stochastic Processes in Physics and Chemistry*; Elsevier Science B.V.: Amsterdam, The Netherlands, 1992.

(10) Feng, F.; Akkutlu, I. Y. *SPE Asia Pacific Unconventional Resources Conference and Exhibition*; Society of Petroleum Engineers: Richardson, TX, 2015.

(11) Wang, S.; Javadpour, F.; Feng, Q. Molecular Dynamics Simulations of Oil Transport through Inorganic Nanopores in Shale. *Fuel* **2016**, *171*, 74−86.

(12) Jin, Z.; Firoozabadi, A. Flow of Methane in Shale Nanopores at Low and High Pressure by Molecular Dynamics Simulations. *J. Chem. Phys.* **2015**, *143*, 104315.

(13) Jin, Z.; Firoozabadi, A. Phase Behavior and Flow in Shale Nanopores from Molecular Simulations. *Fluid Phase Equilib.* **2016**, *430*, 156−168.

(14) Riewchotisakul, S.; Akkutlu, I. Y. Adsorption-Enhanced Transport of Hydrocarbons in Organic Nanopores. *SPE Journal* **2016**, *21*, 1960−1969.

(15) Wang, S.; Javadpour, F.; Feng, Q. Fast Mass Transport of Oil and Supercritical Carbon Dioxide through Organic Nanopores in Shale. *Fuel* **2016**, *181*, 741−758.

(16) Joseph, S.; Aluru, N. Why are Carbon Nanotubes Fast Transporters of Water? *Nano Lett.* **2008**, *8*, 452−458.

(17) Ho, T. A.; Papavassiliou, D. V.; Lee, L. L.; Striolo, A. Liquid Water Can Slip on a Hydrophilic Surface. *Proc. Natl. Acad. Sci. U. S. A.* **2011**, *108*, 16170−16175.

(18) Ungerer, P.; Collell, J.; Yiannourakou, M. Molecular Modeling of the Volumetric and Thermodynamic Properties of Kerogen: Influence of Organic Type and Maturity. *Energy Fuels* **2015**, *29*, 91−105.

(19) Chen, X.; Cao, G.; Han, A.; Punyamurtula, V. K.; Liu, L.; Culligan, P. J.; Kim, T.; Qiao, Y. Nanoscale Fluid Transport: Size and Rate Effects. *Nano Lett.* **2008**, *8*, 2988−2992.

(20) Kannam, S. K.; Todd, B. D.; Hansen, J. S.; Daivis, P. J. How Fast Does Water Flow in Carbon Nanotubes? *J. Chem. Phys.* **2013**, *138*, 094701.

(21) Falk, K.; Sedlmeier, F.; Joly, L.; Netz, R. R.; Bocquet, L. Molecular Origin of Fast Water Transport in Carbon Nanotube Membranes: Superlubricity Versus Curvature Dependent Friction. *Nano Lett.* **2010**, *10*, 4067−4073.

(22) Plimpton, S. Fast Parallel Algorithms for Short-Range Molecular Dynamics. *J. Comput. Phys.* **1995**, *117*, 1−19.

(23) Jones, J. E. On the determination of molecular fields. I. From the variation of the viscosity of a gas with temperature. *Proc. R. Soc. London, Ser. A* **1924**, *106*, 441−462.

(24) Nosé, S. A Unified Formulation of the Constant Temperature Molecular Dynamics Methods. *J. Chem. Phys.* **1984**, *81*, 511−519.

(25) Shinoda, W.; Shiga, M.; Mikami, M. Rapid Estimation of Elastic Constants by Molecular Dynamics Simulation Under Constant Stress. *Phys. Rev. B: Condens. Matter Mater. Phys.* **2004**, *69*, 134103.

(26) Firoozabadi, A. *Thermodynamics of Hydrocarbon Reservoirs*; McGraw-Hill: New York, 1999.

DOI: 10.1021/acs.jpcc.7b09811
J. Phys. Chem. C 2017, 121, 28527−28536

(27) It is known that including flexible nanotube walls has a negligible effect on the results.[41]
(28) Jorgensen, W. L.; Maxwell, D. S.; Tirado-Rives, J. Development and Testing of the OPLS All-Atom Force Field on Conformational Energetics and Properties of Organic Liquids. *J. Am. Chem. Soc.* **1996**, *118*, 11225−11236.
(29) Kaminski, G. A.; Friesner, R. A.; Tirado-Rives, J.; Jorgensen, W. L. Evaluation and Reparametrization of the OPLS-AA Force Field for Proteins via Comparison with Accurate Quantum Chemical Calculations on Peptides. *J. Phys. Chem. B* **2001**, *105*, 6474−6487.
(30) We have applied Kong's mixing rule to obtain the LJ parameters for the methane−carbon interaction.[42]
(31) Kou, R.; Alafnan, S. F. K.; Akkutlu, I. Y. Coupling of Darcy's Equation with Molecular Transport and Its Application to Upscaling Kerogen Permeability. *SPE Europec featured at 78th EAGE Conference and Exhibition*; Society of Petroleum Engineers: New York, 2016; SPE-180112-MS.
(32) Wang, J.; Yang, Z.; Dong, M.; Gong, H.; Sang, Q.; Li, Y. Experimental and Numerical Investigation of Dynamic Gas Adsorption/Desorption−Diffusion Process in Shale. *Energy Fuels* **2016**, *30*, 10080−10091.
(33) It is necessary to mention that, considering $\sim 10^6$ molecules, fluctuations in this linear behavior are tractable.
(34) For the effusion problem between two ideal gases through a channel of radius R, the overall particle flow becomes independent of the channel length and is given by

$$J_{\text{eff}} = \sqrt{\frac{\pi}{2M_{\text{m}}k_{\text{B}}T}}(\Delta P)R^2$$

where M_{m} is the molecular mass.
(35) Cunningham, R. E.; Williams, R. J. J. *Diffusion in Gases and Porous Media*; Plenum Press: New York, 1980.
(36) When $K_{\text{n}} \gg 1$ and considering diffusive reflections with the tube wall, the overall particle flow rate is given by the Knudsen equation

$$J_{\text{knud}} = \frac{2}{3}\sqrt{\frac{8\pi}{2M_{\text{m}}k_{\text{B}}T}}\frac{\Delta P}{L}R^3$$

(37) In our case this characteristic length is near 0.4 nm, and in fact, already for $R \approx 0.5$ nm, we find a non-negligible flow.
(38) It should be noticed that the bin widths of the histograms in Figure 10 are nonuniform, so although these histograms are helpful to show the global picture, some caution is needed which concerns a direct comparison of density values near the wall, since the curvature effect (the adsorption is more pronounced in small radius channels) together with the referred different bin widths (particularly affecting the cases of large radius channels) makes nontrivial the performance of a quantitative comparison of these values among different histograms.
(39) Gonzalez, M. H.; Bukacek, R. F.; Lee, A. L. The Viscosity of Methane. *SPEJ, Soc. Pet. Eng. J.* **1967**, *7*, 75−79.
(40) Majumder, M.; Chopra, N.; Hinds, B. J. Mass Transport through Carbon Nanotube Membranes in Three Different Regimes: Ionic Diffusion and Gas and Liquid Flow. *ACS Nano* **2011**, *5*, 3867−3877.
(41) Alexiadis, A.; Kassinos, S. Molecular Simulation of Water in Carbon Nanotubes. *Chem. Rev.* **2008**, *108*, 5014−5034.
(42) Kong, C. L. Combining Rules for Intermolecular Potential Parameters. II. Rules for the Lennard-Jones (12−6) Potential and the Morse Potential. *J. Chem. Phys.* **1973**, *59*, 2464−2467.

DOI: 10.1021/acs.jpcc.7b09811
J. Phys. Chem. C 2017, 121, 28527−28536